

Analysis of Edge Mismatch and Output Power Degradation in Cascoded Class-D Power Amplifiers Using Dual-Range Voltage Level Shifters

Behdad Jamadi, *Student Member, IEEE*, Meysam Sohani Darban, *Student Member, IEEE*, Jeffrey Sean Walling, *Senior Member, IEEE*.

Abstract—This paper presents a low-jitter hybrid voltage level shifter (HVLS) suitable for high-speed applications. The proposed architecture offers the advantage of cross-coupled feedback to simultaneously generate two voltage domain signals with available swings equal to the nominal supply and its double, which operate up to 12.4 GHz. A prototype HVLS circuit, along with impedance matching and a driver to enable high-speed off-chip testing, was fabricated in a 22-nm FD-SOI process technology. The prototype consumes a total die area, including the interface circuitry, of $477 \times 462 \mu\text{m}^2$, while the active area of the level-shifter is $2 \times 3.26 \mu\text{m}^2$. The average power consumption of the circuit is measured to be $4.43 \mu\text{W}$ per cycle, and the jitter is less than 150 fs-rms.

Index Terms—Class-D PA, differential voltage level shifter (VLS), high-speed level shifter, low-jitter.

I. INTRODUCTION

Recent advancements in CMOS technology have enabled the realization of transistors with significantly reduced parasitic capacitances, resulting in improved switching speeds and higher achievable operating frequencies, particularly in digital circuits. These technological improvements have further facilitated the adoption of multi-level supply voltage architectures in digital and mixed-signal integrated circuits, thereby enhancing overall system performance across diverse applications. A key advantage of such voltage-scaling and multi-domain supply schemes is the reduction of dynamic power consumption, which remains a critical design parameter in energy-efficient integrated systems.

In modern circuits where various functional modules operate under different voltage domains, reliable signal interfacing between sub-blocks necessitates the inclusion of voltage level shifters (VLSs). The VLS serves as an essential interface circuit that translates logic levels from a lower voltage domain—such as subthreshold or nominal levels—to higher voltage domains that are compatible with subsequent circuit stages. As contemporary system-on-chip (SoC) architectures may incorporate a large number of such level shifters, optimizing their power consumption, propagation delay, and silicon area has become a major design consideration [1–3].

Moreover, as CMOS technology continues to scale, the performance improvement in digital circuits is not equally

This work was supported by the National Science Foundation (NSF) under grant #2314813 and GlobalFoundries' University Partner Program. (Corresponding author: Behdad Jamadi, e-mail: behdadjamadi@vt.edu). The authors are with the Bradley Department of Electrical and Computer Engineering, Virginia Tech, Blacksburg, VA 24061 USA. Behdad Jamadi and Meysam Sohani Darban contributed equally to this work.

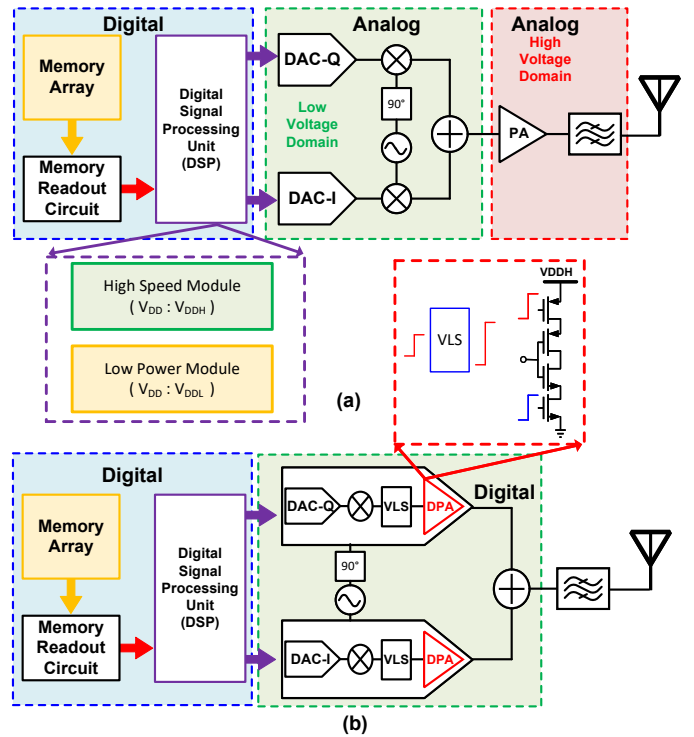


Fig. 1: SoC architectures: a) conventional SoC made of analog and digital blocks and b) modern digital SoC all blocks are made of digital gates.

reflected in analog and RF counterparts due to the reduction in intrinsic gain and output impedance. Consequently, circuit techniques that exploit the switching behavior of transistors have attracted significant attention. Architectures such as digital power amplifiers and fully digital RF transceivers leverage this switching-mode operation to benefit directly from CMOS scaling [4, 5]. Therefore, many next generation SoCs are substituting traditional analog transceiver blocks with fully digital RF transceivers. An overview of a modern SoC integrating both digital and analog subsystems is illustrated in Fig. 1.

One such example of analog block which is designed fully with digital switching circuits is the switched-capacitor power amplifier (SCPA). The output stage of the SCPA is an inverter-based class-D power amplifier (PA) that faces challenges with increasing output power [6]. This limitation arises because class-D PAs use PMOS switches tied to the supply. This restricts the voltage swing, unlike inductor-biased topologies. To support larger output voltage swings, SCPAs and related

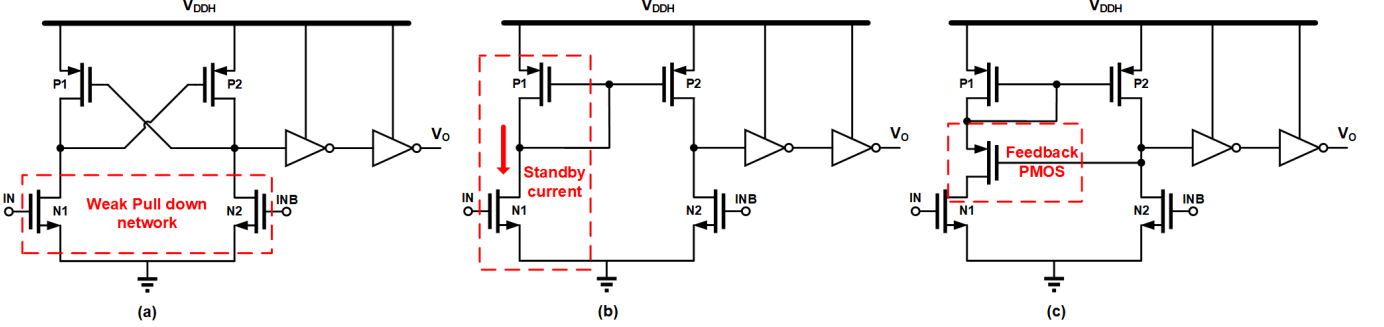


Fig. 2: Schematic of a) Type I: DCVS-based VLS; b) Type II: CM-based VLS; and c) WCMLS.

class-D PAs often use cascoded/stacked inverters, allowing operation at up to $2\times$ the nominal supply voltage when transistor gates are driven appropriately [4, 6]. This approach enhances output power and efficiency, but requires a voltage-level shifter (VLS) to drive the upper PMOS transistor.

A key challenge in such cascoded topologies is synchronizing the signals driving the PMOS and NMOS transistors. The PMOS typically switches between V_{DD} and $2V_{DD}$, while the NMOS switches between GND and V_{DD} . Previous solutions employed programmable delay chains [4, 6]; however, these are sensitive to process-voltage-temperature (PVT) variations and require calibration circuitry, increasing power, area, and complexity. In addition, limited choices of high-speed VLS precludes the design of a high-speed cascode class-D topology.

To overcome these limitations, this work introduces a low-jitter, power-efficient hybrid voltage-level shifter (HVLS) capable of generating both required voltage levels simultaneously while operating at > 12.4 GHz. Its speed and efficiency make it suitable for emerging FR3-band transceivers in next-generation wireless systems.

This paper is organized as follows: Section II reviews VLS topologies and compares the performance of various VLS types, while in its following section, Section III, synchronization effects of utilizing VLS in stacked class-D PAs were analyzed. Moreover, Section IV describes the proposed design. Section VI presents measurement results, and Section VII concludes the work.

II. REVIEW OF VOLTAGE LEVEL-SHIFTERS (VLS)

Most previously proposed VLSs can be classified into three primary architectural families [7, 8]. Among them, the differential cascade voltage shifter (DCVS), shown in Fig. 2 (a), represents a widely used topology [9]. This circuit comprises a pull-up stage formed by a cross-coupled PMOS pair, which acts as a regenerative latch, and a differential NMOS pair that serves as the pull-down network.

One of the key drawbacks of this structure arises from the fact that the input NMOS transistors operate with gate voltages limited to the lower supply domain (V_{DDL}), which is considerably smaller than the higher domain (V_{DDH}). Under comparable sizing between the NMOS and PMOS devices—despite their intrinsic mobility difference—the pull-up path tends to deliver a stronger current than the pull-down path. This imbalance introduces significant contention current between the two networks, particularly when V_{DDL}

approaches the subthreshold region, resulting in degraded switching behavior and increased static power.

This problem ultimately limits the conversion range of the voltage level shifter. In fact, either the NMOSs should be significantly larger, which most of the time is not possible, or the range of available values for V_{DDL} will be reduced. To overcome this issue, [10] proposed a current limiter technique to reduce the pull-up current. While the proposed solution does mitigate the contention current when compared to DCVS topologies, it degrades the output swing due to the lower current. The limited swing inverter in [11] reduces power but suffers from incomplete pull-up transitions, resulting in static current loss [12].

Another architecture that has been proposed is the current mirror-based level shifter (CM), which is shown in Fig. 2 (b). In this circuit, a current mirror configuration has been used instead of the PMOS cross-coupled latch to resolve the current contention issue mentioned before [3, 7, 8]. However, this architecture suffers from a large standby current that passes through the diode-connected PMOS, resulting in more static power consumption. Several alternative designs have been proposed to balance this issue. Stacked devices with various threshold voltages are used in [11] to reduce contention, but this weakens the pull-up network and limits delay scaling when V_{DDL} and V_{DDH} are close. The design in [13] introduces current mismatch circuitry to decouple signal paths; however, contention during high-to-low transitions still increases power and delay. A pre-amplifier-based approach in [14] improves robustness by amplifying mismatches before regeneration; however, intermediate voltage nodes slow down transitions and increase area.

The third topology with significant enhancement is the Wilson current mirror-based level shifter (WCMLS), as shown in Fig. 2 (c) [15, 16]. To suppress the standby current, a feedback PMOS transistor is introduced as a control switch between the NMOS and the diode-connected PMOS device. When the output node goes high, this voltage automatically turns the feedback transistor off, effectively cutting off the static current path and minimizing static power consumption. Despite its advantage in reducing leakage, this configuration introduces two additional key concerns. First, because the current flowing through the mirror branch becomes substantially smaller, the available output current is reduced, leading to a drop in the output voltage. Second, the gate node of the feedback PMOS may become floating under certain conditions, potentially

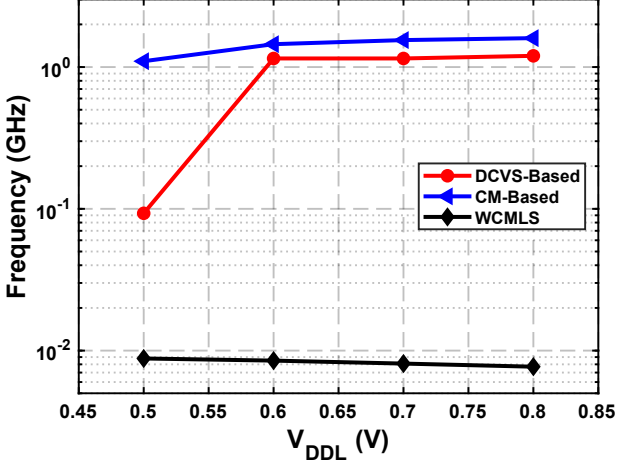


Fig. 3: Maximum operation frequency of the three types of VLSs by adjusting the input voltage (V_{DDL}).

degrading the stability and robustness of the circuit operation. Hybrid architectures in [17, 18] combine current mirror and cross-coupled schemes, yet still experiences contention during switching despite the improvement of the delay and frequency of operation.

To explore the performance and limitations of the conventional VLSs, the main topologies described above have been simulated using a 22-nm FD-SOI technology. The first performance parameter is the operating frequency of each type of VLS as a function of input voltage (V_{DDL}). Fig. 3 illustrates the maximum operation frequency of the aforementioned three architectures versus the input voltage (V_{DDL}). The frequency of operation for the WCMLS is significantly lower than the DCVS and CM-based VLS and is limited to a few MHz. However, the CM-based and DCVS-based perform in a similar frequency range for most of the input voltage range.

The propagation delay and power consumption of the conventional VLSs are illustrated in Fig. 4 regarding the input voltage level. The power consumption of the CM-based VLS is higher than that of others for most input voltage levels due to the static current during transitions. In contrast, the WCMLS consumes significantly less current due to the current limiter feedback transistor. Within the input voltage range, the power consumption of the DCVS-based level shifter surpasses that of the CM-based counterpart. This higher power dissipation arises from contention currents that occur when both pull-up and pull-down transistors operate simultaneously in the saturation region.

Besides the power consumption, the propagation delay of the VLSs is highlighted in Fig. 4. The CM-based VLS incurs higher power consumption; however, it provides the advantage of reduced propagation delay. In contrast, the propagation delay of WCMLS is higher by an order of magnitude than that of CM-based due to the limited current drawn from the supply for the transition. It is worth noting that the performance of the DCVS-based level shifter is dependent on the input voltage, where both propagation delay and power consumption decrease as the input voltage increases where highlighted by the red lines in Fig. 4. A key observation regarding the propagation delay of the DCVS-based level shifter is that it can

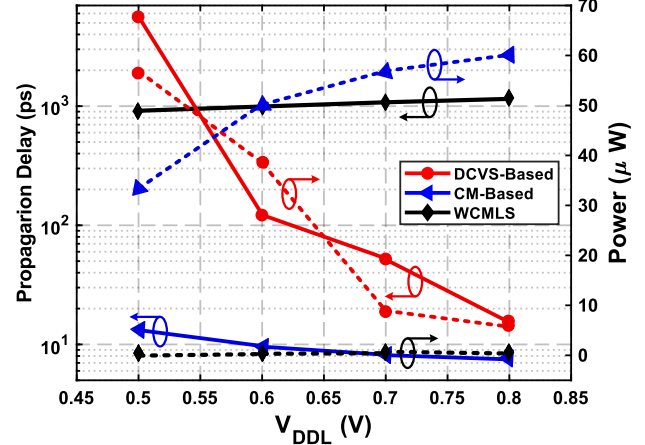


Fig. 4: Propagation delay and power consumption of the three types of VLSs by adjusting input voltage.

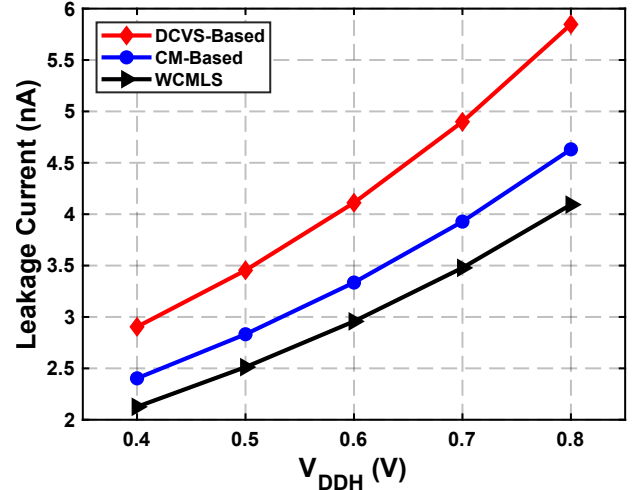


Fig. 5: Leakage current of the three types of VLSs by adjusting their supply.

decrease by nearly three orders of magnitude when the input voltage increases from 0.5 V to 0.8 V, which was expected since the current of the NMOS pair is relative to the input voltage in this topology.

A comparison of the leakage current of three types of level shifters can also be seen in Fig. 5, which demonstrates how leakage current varies as a function of supply voltage. As the figure shows, The leakage current of the DCVS-based VLS is higher compared to other architectures and can increase to approximately 6 nA as the supply voltage rises to 0.8 V. WCMLS has the lowest leakage current thanks to the feedback transistor that can increase the effective length in the leakage path.

From these studies, five key VLS design criteria emerge:

- 1) Minimized contention current for efficient conversion,
- 2) Fast transition speed under low input voltages,
- 3) Zero static current at internal nodes to reduce power,
- 4) Compact area with minimal device count, and
- 5) Scalable delay as supply levels converge.

The level-shifter proposed in this article is optimised for both SoC integration and high-speed digital PAs, addressing all

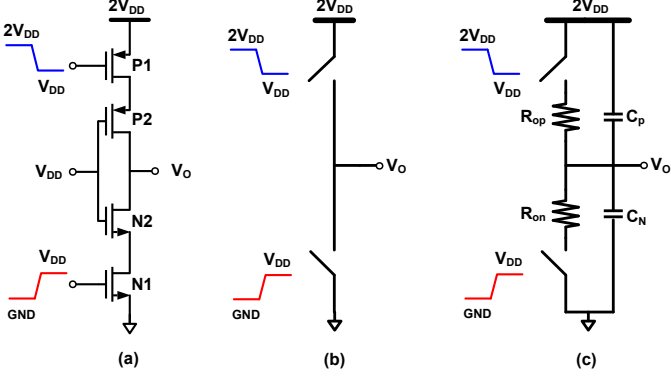


Fig. 6: Stacked class-D PA: a) schematic, b) ideal model, and c) non-ideal model.

the above requirements. Unlike prior art, existing VLS designs fail to meet these criteria simultaneously, particularly when driving stacked class-D PAs in SCPA circuits. The analysis of delay mismatch in the cascaded class-D PA is presented in the following section, considering two distinct operating scenarios in order to highlight the importance of the high-speed VLS for the Digital amplifiers.

III. DELAY MISMATCH EFFECT ON OUTPUT POWER

The delay mismatch between the PMOS and NMOS switching signals introduces duty cycle distortion on circuits such as class-D PAs. In particular, this effect becomes critical in cascaded/stacked inverter-based topologies, where the reduced output pulse width degrades overall performance. To evaluate this impact, two scenarios are considered: an ideal cascode class-D PA, whose transistors are modeled as ideal switches, and a non-ideal case incorporating realistic device and interconnect delay.

A. Case Study I: Ideal Cascode Class-D PA

Under ideal conditions, the switches have a very low resistance, and the impedance of NMOS and PMOS is considered equal for a cascode class-D PA, as shown in Fig. 6 (b). For the ideal case that signals are synchronized, in Fig. 7 (a), the output power of the class-D PA with double of nominal supply voltage is calculated according to the first Fourier coefficient [19]:

$$P_{out,i} = \frac{8}{\pi^2} \cdot \frac{V_{DD}^2}{R_{opt}} \quad (1)$$

where $P_{out,i}$ and R_{opt} are the output power of the stacked class-D PA and the optimum resistance seen from the matching network, respectively.

Therefore, the delay mismatch in toggling the gate voltage of P1 and N1 results in a two-level step signal waveform shown in Fig. 7 (b). The output signal has a voltage level of $2 \cdot V_{DD}$, with a pulse width of $T_c - T_{ms}$ where T_c is the carrier frequency, and T_{ms} presents the time mismatch between signals driving PMOS and NMOS

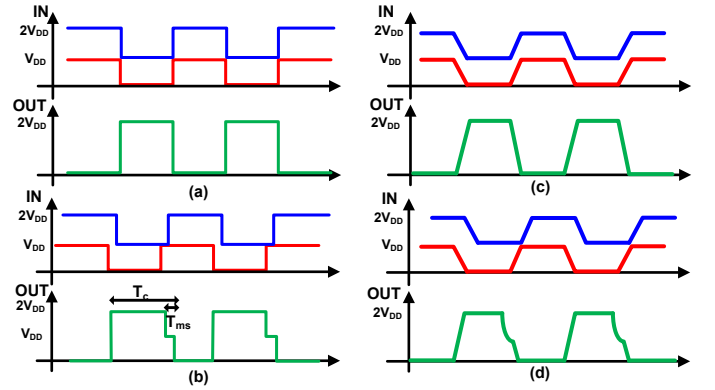


Fig. 7: Waveforms for cascaded class-D PA using an ideal switch model when driven by: a) ideally synchronous signals, and b) signals with delay mismatch driving signal. Using a non-ideal switch model when driven by: c) ideally synchronous signals, and d) signals with delay mismatch.

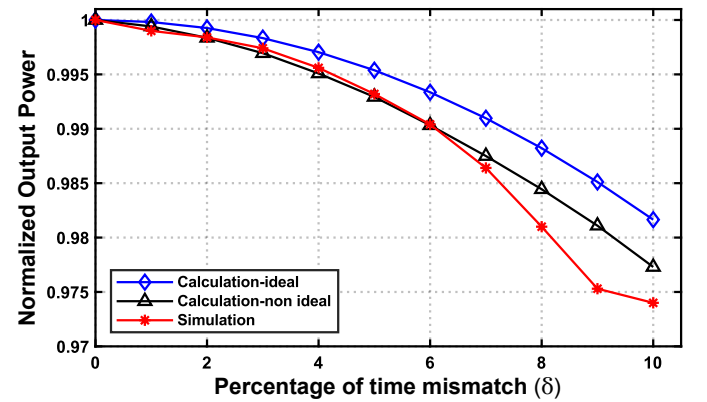


Fig. 8: Output power degradation of the stacked class-D PA in comparison with the percentage of the delay mismatch.

in cascode class-D PA. Hence, the output power of a stacked class-D PA under delay mismatch can be calculated as follows:

$$P_{out,ni} = P_{out,i} \cdot \left[\sin^2(\pi \cdot (\frac{1}{2} - \delta t)) + \frac{1}{4} \cdot \sin^2(\frac{\pi}{2} \delta t) \right] \quad (2)$$

where

$$\delta t = \frac{T_{ms}}{T_c} \quad (3)$$

and $P_{out,ni}$ indicates the output power under the delay mismatch condition, where the second term in (2) shows the roots of power degradation due to the delay mismatch of driving signals.

B. Case Study II: Non-Ideal Cascode Class-D PA

In realistic conditions, the switches' output resistance and parasitic capacitance are not negligible. They must be considered in the model for a stacked inverter in class-D PA, depicted in Fig. 6 (c). These non-ideality forms a time constant at the output that impedes the output voltage division from occurring, similar to the ideal condition. In addition, in these conditions, there is no abrupt toggling between supply rails in the inverter; therefore, the rise time and fall time play an imperative role

in modeling the delay mismatch of signals driving the PMOS and NMOS in stacked inverters. The time constant, τ , at the output of the cascode inverters is defined as the product of R_{out} and C_{out} . The output resistance of the cascode inverters is approximated as follows:

$$R_{out} = R_{on} \parallel R_{op} \quad (4)$$

where $R_{op/on}$ is equivalent to:

$$R_{op/on} = r_{o1,n/p} + r_{o2,n/p} + g_{m1,n/p} \cdot r_{o1,n/p} \cdot r_{o2,n/p} \quad (5)$$

Here, r_o denotes the output resistance of the FET transistors during the output transition phase, wherein both devices operate in the saturation region. Furthermore, the output capacitance of the cascode inverter is primarily determined by the parasitic capacitance associated with the intrinsic properties of the MOSFET devices.

$$C_{out} = c_{gd,n} \cdot (1 + Av^{-1}) + c_{gd,p} \cdot (1 + Av^{-1}) \quad (6)$$

Where A_v is the intrinsic gain of the FET devices. Thus, considering the introduced τ during the transition of output, now the delay mismatch needs to be evaluated during the rise time and/or fall time. In contrast to the ideal condition, the effect of delay mismatch in a non-ideal condition is modeled as a charge/discharge of a single-order RC circuit during the time that both NMOS and PMOS are ON due to the delay mismatch. Therefore, assuming the delay mismatch is comparable to the rise-time and fall-time of the cascoded inverter, the transition between the rails can be presented as a combination of a ramp and an exponential signal, Fig. 7 (d). Hence, now the fundamental coefficient of the Fourier transform of the signal can be presented as the summation of the first Fourier transform coefficient of all the sections of the signal, including the step signal, exponential, C_{exp} , and ramp signal, C_{rmp} during the transition of output, which occurs because of time mismatch.

$$C_{rmp} = \frac{2\Delta V}{\Delta t \cdot T^2} \cdot \frac{e^{-j2\pi\Delta t}(j2\pi\Delta t - 1) + 1}{(j\omega)^2} \quad (7)$$

and,

$$C_{exp} = \frac{2\Delta V}{T} \cdot \left[\frac{1 - e^{j\omega\Delta t \cdot T}}{j\omega} - \frac{1 - e^{\Delta t \cdot T(1/\tau + j\omega)}}{1/\tau + j\omega} \right] \quad (8)$$

where ω is the frequency of the signal, Δt and ΔV represent the period of each signal and the voltage variation of each section.

Fig. 8 presents a comparison between the analytical model and transistor-level simulation results, highlighting the impact of delay mismatch on the normalized output power. As observed, the output power decreases by approximately 3% as the delay mismatch increases from 0% to 10% of the carrier period. This trend suggests that even minor mismatches become increasingly significant at higher operating frequencies, resulting in more pronounced performance degradation. Due to the significance of the mismatch in the switching signals provided by VLS, and the performance comparison and issues described in Section II, a novel VLS has been proposed, which is detailed in the following section.

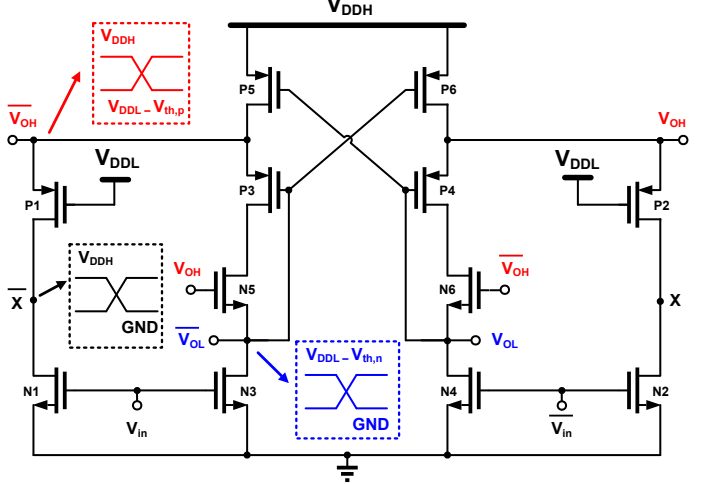


Fig. 9: Schematic of proposed HVLS.

IV. PROPOSED HYBRID VOLTAGE LEVEL SHIFTER

The schematic and supported voltage transitions of the proposed HVLS are illustrated in Fig. 9. To address limitations in earlier designs (Section II), the architecture integrates multiple enhancement techniques. A cross-coupled PMOS pair (P5–P6) accelerates output transitions, while diode-connected PMOS devices (P3–P4), placed in series with N5–N6, mitigate current contention. These NMOS devices also serve as cross-coupled transistors, with their gates tied to $\overline{V_{OH}}$ and V_{OH} , thereby improving transition sharpness and enhancing the regenerative latch effect. Additionally, P1 and P2 limit the contention current in the leftmost and rightmost branches.

The level shifting mechanism is as follows: when V_{in} transitions from ground to V_{DDL} , N1 and N3 activate, pulling down $\overline{V_{OL}}$ and \overline{X} to 0 V. With node \overline{X} initially at V_{DDH} , N1 operates in strong inversion once $V_{in} = V_{DDL}$. However, the discharge of V_{OH} is constrained to $V_{DDL} - V_{th,p}$ due to P1's gate bias. Concurrently, N3 discharges $\overline{V_{OL}}$ and activates P6, which charges V_{OH} and X to V_{DDH} . The rise in V_{OH} turns on N5, which assists N3 in discharging $\overline{V_{OL}}$ more quickly. An analogous process occurs on the complementary path when $\overline{V_{in}}$ rises. Nodes X and \overline{X} swing between ground and V_{DDH} , while V_{OH} , $\overline{V_{OH}}$, V_{OL} , and $\overline{V_{OL}}$ operate between $V_{DDL} - V_{th,p}$ and $V_{th,n}$. Biasing P1 and P2 gates at V_{DDL} prevents overstress on P5 and P6 at elevated supply voltages. Additionally, diode-connected P3 and P4 lower the impedance at V_{OH} and $\overline{V_{OH}}$, enhancing speed. The regenerative cross-coupled structure introduces a strong negative input resistance during transitions, which leads to fast, low-jitter output behaviour.

To analyze this negative resistance and performance of the circuit, we define the following substitutions for compactness:

$$A = g_{m,p3}r_{o,p3}, \quad B = g_{m,n5}r_{o,n5}, \quad C = g_{m,p5}r_{o,p5}, \quad (9)$$

With these definitions, the equivalent resistance can be expressed as

$$R_{eq}(A, B) \approx -2 \times \frac{R_0 + r_{o,p5}(A - B)}{A - C - B + CB - AC}, \quad (10)$$

where

$$R_0 = r_{o,p3} + r_{o,n5} + r_{o,p5}. \quad (11)$$

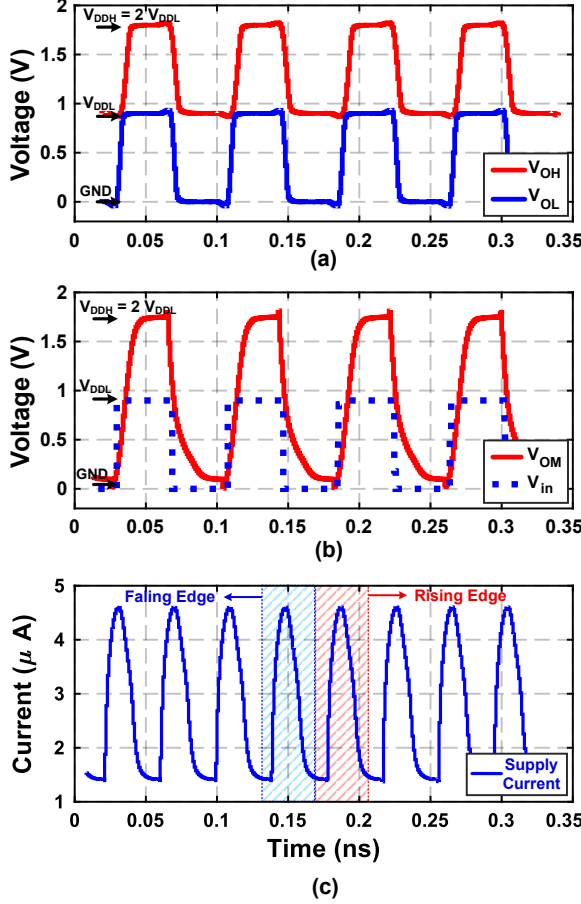


Fig. 10: Simulation of (a) V_{OH} and V_{OL} and (b) Output voltages and (c) supply current waveform.

The denominator of (10) can be simplified as

$$A - C - B + CB - AC = (1 - C)(A - B) - C. \quad (12)$$

Introducing the difference variable

$$\Delta = A - B, \quad (13)$$

(10) reduces to the fractional-linear form

$$R_{eq}(\Delta) = -2 \times \frac{R_0 + r_{o,p5}\Delta}{(1 - C)\Delta - C}. \quad (14)$$

To have a strong positive feedback in order to reduce the jitter, the denominator should approach to zero. Therefore, it infers that the Δ should be equal to:

$$\Delta = \frac{C}{1 - C}. \quad (15)$$

The analysis demonstrates that the correct sizing of N5 and P3 can lead to strong positive feedback, resulting in a low jitter HVLS. The negative resistance seen at N3 and N4 is given by (16), where $g_{m,(p/n)i}$ and $r_{o,(p/n)i}$ are the corresponding transconductance and channel length modulation resistance of the transistors in the proposed HVLS.

$$R_{eq} \approx -2 \times \frac{r_{o,p3} + r_{o,n5} + r_{o,p5} + g_{m,p3} \cdot r_{o,p3} \cdot r_{o,p5} - g_{m,n5} \cdot r_{o,n5} \cdot r_{o,p5}}{g_{m,p3} \cdot r_{o,p3} - g_{m,p5} \cdot r_{o,p5} - g_{m,n5} \cdot r_{o,n5} + g_{m,p5} \cdot r_{o,p5} \cdot g_{m,n5} \cdot r_{o,n5} - g_{m,p3} \cdot r_{o,p3} \cdot g_{m,p5} \cdot r_{o,p5}} \quad (16)$$

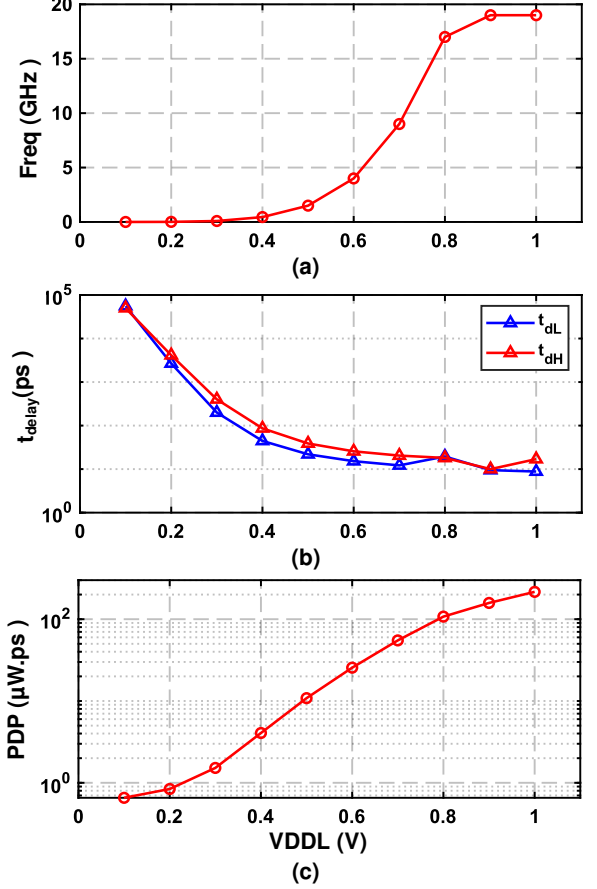


Fig. 11: (a) Maximum operating frequency, (b) propagation delays, and (c) PDP of HVLS at maximum operation frequency over different supplies ($V_{DDH} = 2V_{DDL}$).

V. FUNCTION OF HVLS FOR ANALOG AND DIGITAL APPLICATIONS

As illustrated in Fig. 1, the utilization of the proposed HVLS extends beyond digital signal processing (DSP) modules, serving a crucial function in the analog front end of system-on-chip (SoC) architectures. Accordingly, the performance of the HVLS is further evaluated in both digital circuits employed within DSP blocks and in cascoded class-D amplifiers, which constitute essential components of digital transmitters and analog front ends.

A. The Analog Application Simulation Results of the Proposed HVLS

To corroborate the analytical results, post-layout simulations were performed in a 22-nm FD-SOI process. The HVLS was excited with the target input waveform, and the corresponding transient responses are illustrated in Fig. 10 (a)–(c). The plots show the voltage transitions at the output nodes as well as the instantaneous current drawn from the supply. The simulation

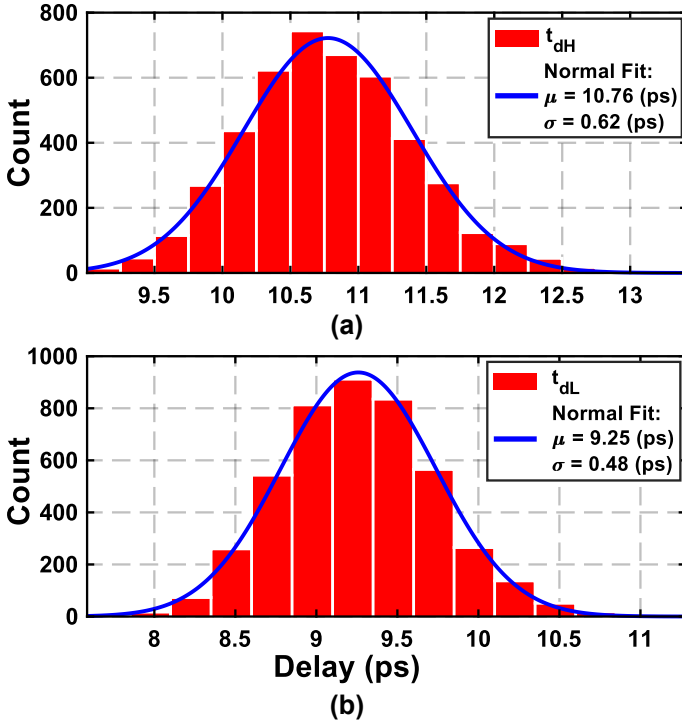


Fig. 12: MonteCarlo simulation of the HVLS for (a) t_{dH} , (b) t_{dL} .

was conducted at a clock frequency of 12.4 GHz under a dual-supply condition of $V_{DDH} = 2V_{DDL}$, where $V_{DDL} = 0.9$ V represents the nominal voltage of the adopted technology.

Simulation results in Fig. 11 confirm high-speed operation, with a supply of $2V_{DDL}$. As shown in Fig. 11 (a), the HVLS supports frequencies up to 19 GHz at V_{DDH} equal to 1.8 V while input is toggled between GND and 0.9 V. Lower supply operation is possible at reduced frequencies and lower power consumption. Fig. 11 (b) displays propagation delays to V_{OH} (t_{dH}) and V_{OL} (t_{dL}), exhibiting good symmetry and flat delay characteristics above 0.6 V. The power-delay product (PDP), plotted in Fig. 11 (c), increases with frequency and voltage, as expected.

To evaluate the robustness of the proposed design, 4500 Monte Carlo simulations were performed on the circuit. Fig. 12 illustrates the Monte Carlo simulation results for the proposed circuit's delays from input to both outputs. The mean delay for the V_{OH} (t_{dH}) is 10.76 ps with a standard deviation of 0.62 ps. Meanwhile, for the other output V_{OL} , the mean delay is 9.25 ps with a standard deviation of 0.48 ps. Considering three times the standard deviation (3σ), the maximum variation of the delay changes by only 1.86 ps in 99.73% of the cases.

B. Digital Application Simulation Results of the Proposed HVLS.

The proposed circuit serves as a high-speed level shifter capable of translating signal amplitudes from a lower voltage domain (V_{DDL}) to a higher voltage domain (V_{DDH}). To evaluate its performance, extensive process corner simulations were conducted. Assuming a constant voltage supply equal to the nominal voltage (0.9 V), Fig. 13 illustrates the maximum

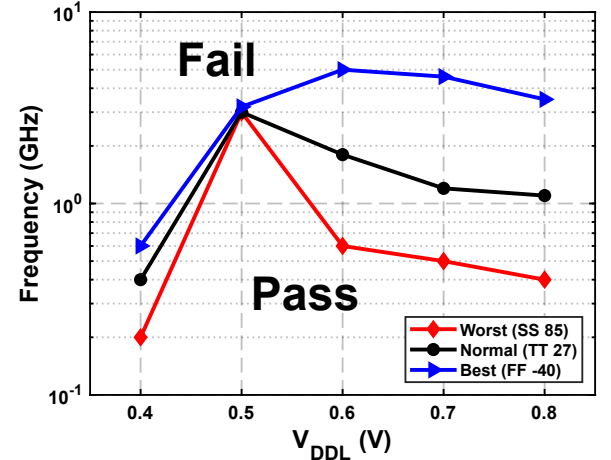


Fig. 13: Maximum operation frequency of the HVLS at different supply voltages over corners.

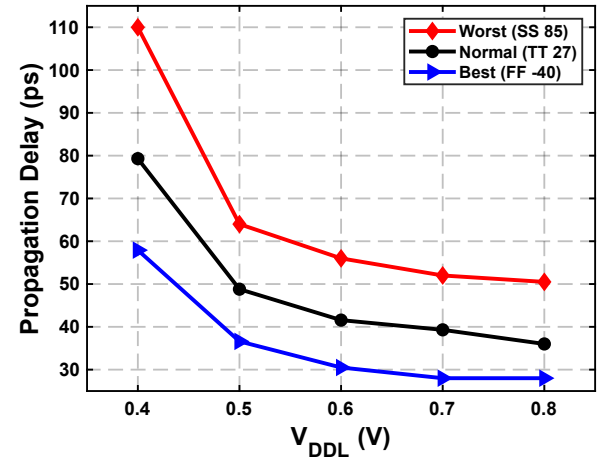


Fig. 14: Propagation delay variation of the proposed circuit at different supply over corners.

operating frequency of the proposed HVLS under different process corners—best (FF, -40°C), worst (SS, 85°C), and Normal (TT, 27°C)—as input voltage V_{DDL} is varied. These simulations were performed to isolate the supply sensitivity of the HVLS, independent of any preceding circuit stage. The results demonstrate that the proposed design maintains reliable operation up to 3.5 GHz at 0.8V at The Best condition, three times exceeding the performance of previously reported level shifters discussed in Section II. The *Pass* region highlighted in Fig. 13 denotes the frequency range over which the circuit achieves correct functionality. Since the proposed high-voltage level shifter (HVLS) integrates both a current-source stage and a positive-feedback network within its architecture, it exhibits maximum operating frequency when the input swing is in the low-voltage range of 0.4–0.5 V. In this region, transistors N1–N4 remain in strong saturation throughout the entire period during which the input signal is high. As the input voltage range increases, however, the duration for which N1–N4 stay in strong saturation decreases, and these devices enter the triode region after the output transition is completed. Consequently, the overall maximum operating speed of the circuit is reduced.

Moreover, Fig. 14 and 15 respectively illustrate the propa-

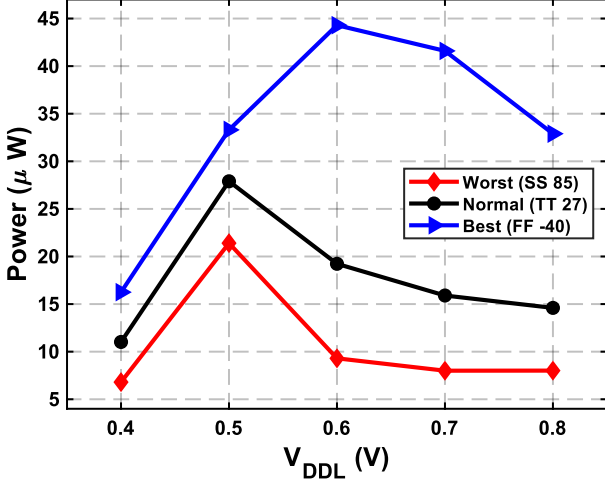


Fig. 15: HVLS's power consumption at different supply over corners.

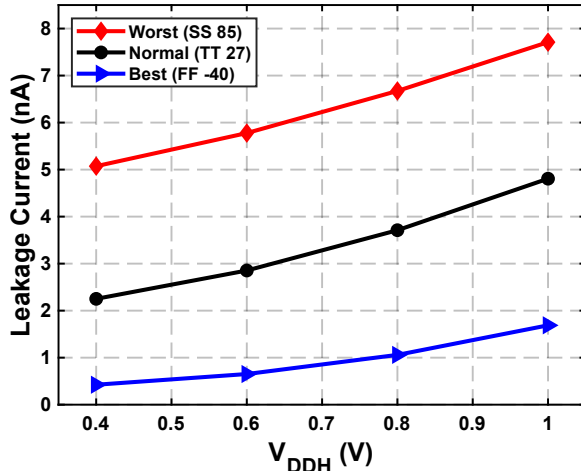


Fig. 16: Leakage current of the HVLS at different supply over corners.

gation delay and power consumption of the designed HVLS in the main three corners and conditions relative to the supply's value. Compared to Fig. 4, the design has less delay, especially at high frequencies. Less delay is achieved due to the presence of the two positive feedbacks employed in this circuit that accelerate the transition and improve the sharpness of signals. Finally, the leakage current of the circuit by adjusting the supply voltage is indicated in Fig. 16. The leakage current of the proposed circuit for a supply voltage of 1 V value is almost

5 nA in normal condition, which is similar to the leakage of the DCVS-based VLS.

VI. MEASUREMENT AND RESULTS

The HVLS prototype was fabricated in 22-nm FD-SOI process technology. For high-speed off-chip testing, a dedicated test circuit was designed with a broadband $50\ \Omega$ input match, as shown in Fig. 17(a). The input RF signal is split into two inverter paths to generate differential pulses, with a transition gate in the positive path for synchronization. The inverter-based structure ensures fast transitions between ground and V_{DDH} . The HVLS outputs drive a differential class-D PA, designed to enable the signal to be driven off-chip and demonstrate the functioning of the HVLS. The half-circuit of the cascaded class-D PA is shown in Fig. 17(b). This class-D circuit was designed as a single "slice" in an SCPA and is solely used to characterise the HVLS's ability to drive its voltage transitions at high speed with a realistic load. To enable off-chip measurements, a transformer-based balun was designed to provide impedance matching around our intended application frequency of ≈ 12.4 GHz. The cell layout and the chip photograph of the prototype are shown in Fig. 17(c). The total chip area, including pads, is $477 \times 462\ \mu\text{m}^2$ while the HVLS itself only occupies $3.264 \times 2\ \mu\text{m}^2$.

Although the transformer at the output limits the measurement bandwidth to the intended operating frequency, simulations confirm that the circuit can function beyond this range (up to 19 GHz). The input and output matching performance is shown in Fig. 18 (a). S_{11} is wide-band due to the resistive matching, and S_{22} is less than -10 dB from 12.1 to 12.5 GHz. Besides, Fig. 18 (b) depicts the measured output spectrum of the circuit when operating at 12.4 GHz. It is essential to note that the low output power depicted in Fig. 18 (b) results directly from the small class-D amplifier (single slice of an SCPA) positioned after the HVLS. This design choice was made deliberately to replicate the actual operational performance of the proposed circuit within an SCPA structure. In a complete SCPA circuit, multiple slices, similar to the one illustrated in Fig. 17 (a), work together to increase output power and apply amplitude modulation, which was not intended in this article. Utilizing a larger PA at the output will increase the load capacitance for the HVLS and ultimately degrade its performance.

The class-D PA in the output operates if the level shifter can provide proper signals with the required voltage levels.

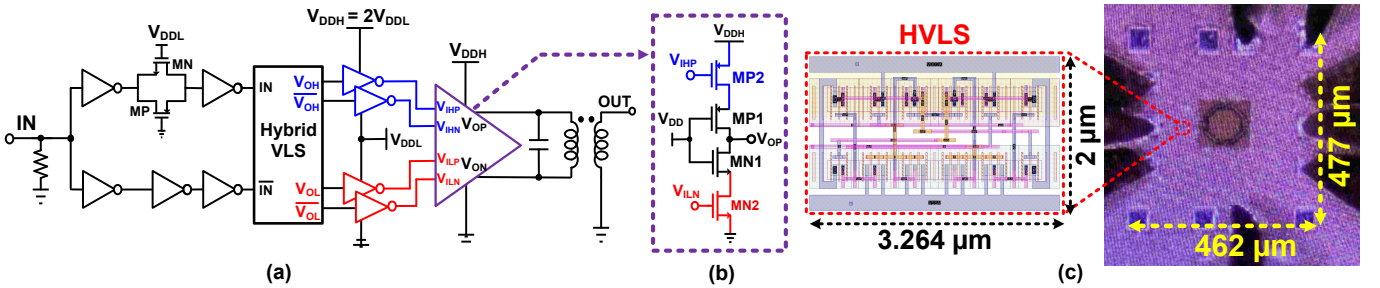
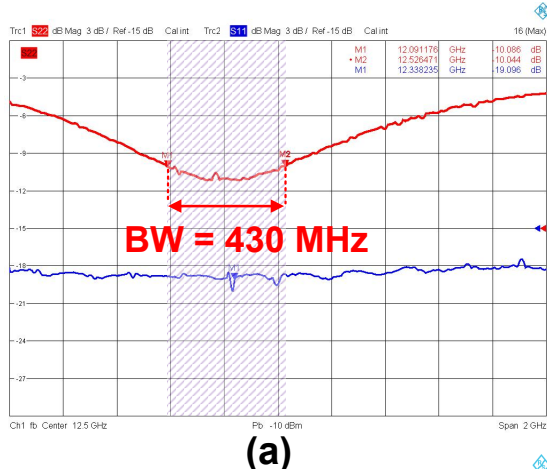


Fig. 17: (a) Schematic of implemented HVLS with input and output drivers, (b) stacked class-D PA, and (c) chip micrograph.

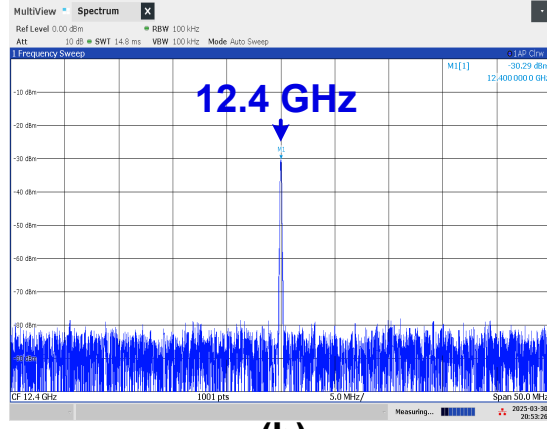
TABLE I: Performance Summary and Comparison with State-of-Art Voltage Level Shifter

Parameter	Technology	VDD _L	VDD _H	Delay (ns)	VDD _{L,min} (V) @Freq	Energy/Trans (fJ)	Area (μm^2)	Static Power	Result
[7]	55 nm	0.3 V	1.2 V	12.1	0.13 @ 100 KHz	16.13 @ 1 MHz	7.94	16.72 pW	Sim.
				13.86	0.15 @ 100 KHz	22.71 @ 1 MHz	7.94	34.8 pW	Meas.
[17]	55 nm	0.3 V	1.2 V	20.08	0.196 @ 1 MHz	18.11 @ 1 MHz	9.98	0.12 nW	Meas.
[20]	65 nm	0.2	1.2	26.75	0.12 @ 1 MHZ	147 @ 10 MHz	6.9	2.66 nW	Meas.
[21]	40 nm	0.3	1.1	80	0.05 @ 1 MHZ	4.2 @ 1 MHz	8	0.55 nW	Meas.
[22]	7 nm	0.4 V	1.2 V	0.21	0.14 @ 1 MHz	18 @ 1 MHz	12	0.6 nW	Meas.
[23]	28 nm FD-SOI	0.2 V	1.0 V	10.1	0.043 @ N/A	5.2 @ 1 MHz	16.6	6.5 nW	Sim.
[24]	28 nm	0.4 V	1.0 V	0.474	0.28 @ N/A	0.743 @ 10 MHz	N/A	13.8 nW	Meas.
This Work	22 nm FD-SOI	0.4 V	0.9	0.521	0.4 @ 160 MHz	0.925 @ 160 MHz	6.528*	78.86 μW	Sim.
		0.9 V	1.8 V	0.012	0.9 @ 12.4 GHz	40.87 @ 12.4 GHz		220 μW	Meas.

*HVLS chip area without drivers, pads, and matching network. Sim.: Simulation result, Meas.: Measurement result.



(a)



(b)

Fig. 18: (a) Input and output matching and (b) output spectrum.

The total jitter for this circuit is 150 fs-rms according to phase noise measurement, which is expected based upon simulation results. Moreover, Fig. 19 indicates the implemented circuit's normalized output power by adjusting its supply by 10%. As expected, the output power decreases by 3 dBs around the bandwidth of the output matching. It is important to mention that the proposed HVLS is able to work in higher frequencies with wider bandwidths; however, since this case is a stand-alone circuit, not a full SCPA, the output bandwidth was limited by the matching network to test and validate the operation. The power consumption breakdown of the prototype design is illustrated in Fig. 20. As shown, only 36% of the power consumption is due to the HVLS, which consumes

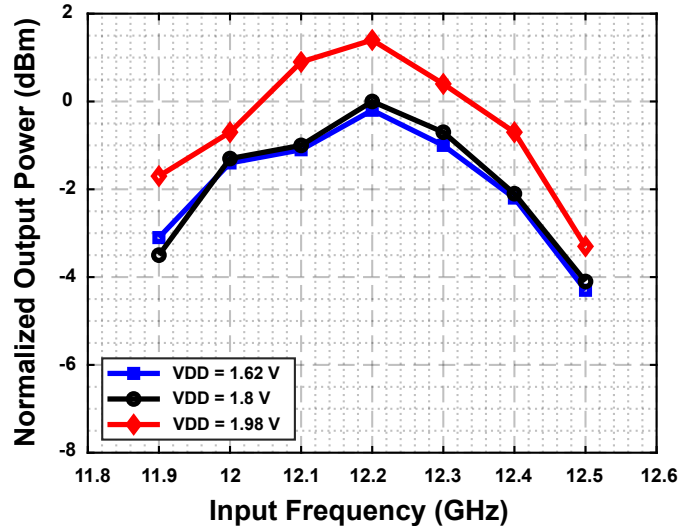
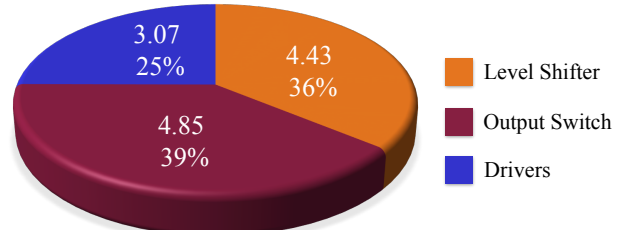


Fig. 19: Normalized measured output power over different frequencies with 10% supply variation.



Total Power per Cycle = 12.35 $\mu\text{W}/\text{cycle}$

Fig. 20: Power breakdown of the total circuit.

4.43 μW per cycle. The balance of power is consumed in the input driver (25%) and the class-D PA output pad driver (39%). A comparison to prior art in level-shifters is shown in Table I. The proposed HVLS operates at higher frequencies and has less delay due to the use of hybrid architecture. For a comparison to lower-frequency results, we add the simulation results at lower frequency operation (160 MHz).

VII. CONCLUSION

This work investigates the effect of PMOS–NMOS drive signal mismatch on the output power of cascaded Class-D power amplifiers (PAs) and presents a novel hybrid voltage

level shifter (HVLS) architecture. The proposed HVLS simultaneously provides two distinct voltage level shifts—one corresponding to the nominal supply and another at twice its value—enabling efficient signal translation for stacked Class-D PA architectures. Owing to its high-speed operation of up to 19 GHz, the HVLS is particularly suitable for driving switch-capacitor power amplifiers (SCPAs) in fully digital transmitter systems. In addition, the proposed design is simulated and evaluated for its applicability in digital signal processing (DSP) modules, and its performance is benchmarked against conventional voltage level shifters (VLSs). The implementation is carried out using a 22-nm FD-SOI process technology and characterized at 12.4 GHz, achieving a power consumption of 4.43 μ W per cycle with a total integrated output jitter of 150 fs.

VIII. ACKNOWLEDGMENT

The authors would like to acknowledge the National Science Foundation (NSF) under grant #2314813 and Global-Foundries' University Partner Program for their support.

REFERENCES

- [1] Y. Li, J. Zhao, Y. Liu, and G. Wang, "A comprehensive study on the design methodology of level shifter circuits," *IEEE Transactions on Circuits and Systems I: Regular Papers*, vol. 70, no. 1, pp. 302–314, 2023. DOI: 10.1109/TCSI.2022.3213981
- [2] H. Jeong, T.-H. Kim, C. N. Park, H. Kim, T. Song, and S.-O. Jung, "A wide-range static current-free current mirror-based LS with logic error detection for near-threshold operation," *IEEE Journal of Solid-State Circuits*, vol. 56, no. 2, pp. 554–565, 2021. DOI: 10.1109/JSSC.2020.3014954
- [3] L. Fassio et al., "A robust, high-speed and energy-efficient ultralow-voltage level shifter," *IEEE Transactions on Circuits and Systems II: Express Briefs*, vol. 68, no. 4, pp. 1393–1397, 2021. DOI: 10.1109/TCSI.2020.3033253
- [4] H. M. Nguyen, J. S. Walling, A. Zhu, and R. B. Staszewski, "A mm-wave switched-capacitor RFDAC," *IEEE Journal of Solid-State Circuits*, vol. 57, no. 4, pp. 1224–1238, 2022. DOI: 10.1109/JSSC.2022.3142718
- [5] J. Zanen, E. Klumperink, and B. Nauta, "Power efficiency model for MIMO transmitters including memory polynomial digital predistortion," *IEEE Transactions on Circuits and Systems II: Express Briefs*, vol. 68, no. 4, pp. 1183–1187, 2021. DOI: 10.1109/TCSI.2020.3028493
- [6] H. M. Nguyen, F. Zhang, I. O'Connell, R. B. Staszewski, and J. S. Walling, "An edge-combining frequency-multiplying class-D power amplifier," *IEEE Transactions on Circuits and Systems II: Express Briefs*, vol. 70, no. 2, pp. 471–475, 2023. DOI: 10.1109/TCSI.2022.3171495
- [7] A. Yuan, H. Zhao, X. Wang, Z. Li, and S. Qiao, "An ultra-low leakage and wide-range voltage level shifter for low-power digital CMOS VLSIs," *IEEE Transactions on Circuits and Systems II: Express Briefs*, vol. 71, no. 3, pp. 1406–1410, 2024. DOI: 10.1109/TCSI.2023.3323016
- [8] H. You, J. Yuan, W. Tang, S. Qiao, and Y. Hei, "An energy-efficient level shifter for ultra low-voltage digital LSIs," *IEEE Transactions on Circuits and Systems II: Express Briefs*, vol. 67, no. 12, pp. 3357–3361, 2020. DOI: 10.1109/TCSI.2020.2980681
- [9] S. Kabirpour and M. Jalali, "A low-power and high-speed voltage level shifter based on a regulated cross-coupled pull-up network," *IEEE Transactions on Circuits and Systems II: Express Briefs*, vol. 66, no. 6, pp. 909–913, 2019. DOI: 10.1109/TCSI.2018.2872814
- [10] M. Lanuzza, F. Crupi, S. Rao, R. De Rose, S. Strangio, and G. Iannaccone, "An ultralow-voltage energy-efficient level shifter," *IEEE Transactions on Circuits and Systems II: Express Briefs*, vol. 64, no. 1, pp. 61–65, 2017. DOI: 10.1109/TCSI.2016.2538724
- [11] W. Zhao, A. B. Alvarez, and Y. Ha, "A 65-nm 25.1-ns 30.7-fJ robust subthreshold level shifter with wide conversion range," *IEEE Transactions on Circuits and Systems II: Express Briefs*, vol. 62, no. 7, pp. 671–675, 2015.
- [12] V. L. Le and T. T.-H. Kim, "An area and energy efficient ultra-low voltage level shifter with pass transistor and reduced-swing output buffer in 65-nm CMOS," *IEEE Transactions on Circuits and Systems II: Express Briefs*, vol. 65, no. 5, pp. 607–611, 2018. DOI: 10.1109/TCSI.2018.2820155
- [13] M. N. Sharifi, H. Rashidian, and N. Shiri, "A 38.5-fJ 14.4-ns robust and efficient subthreshold-to-suprathreshold voltage-level shifter comprising logic mismatch-activated current control circuit," *IEEE T. Circuits Syst. II*, vol. 70, no. 6, pp. 1906–1910, 2023.
- [14] R. Matsuzaka and T. a. Hirose, "An 80-mV-to-1.8-V conversion-range low-energy level shifter for extremely low-voltage VLSIs," *IEEE T. Circuits Syst. I*, vol. 64, no. 8, pp. 2026–2035, 2017.
- [15] S. Lütkemeier and U. Rückert, "A subthreshold to above-threshold level shifter comprising a Wilson current mirror," *IEEE Transactions on Circuits and Systems II: Express Briefs*, vol. 57, no. 9, pp. 721–724, 2010. DOI: 10.1109/TCSI.2010.2056110
- [16] S. Kabirpour and M. Jalali, "A power-delay and area efficient voltage level shifter based on a reflected-output Wilson current mirror level shifter," *IEEE Transactions on Circuits and Systems II: Express Briefs*, vol. 67, no. 2, pp. 250–254, 2020. DOI: 10.1109/TCSI.2019.2914036
- [17] C. Huang and H. Jiao, "C³MLS: An ultra-wide-range energy-efficient level shifter with CCLS/CMLS hybrid structure," *IEEE J. Solid-State Circuits*, vol. 58, no. 10, pp. 2685–2695, 2023.
- [18] S. Ali, S. Tanner, and P. A. Farine, "A robust, low power, high speed voltage level shifter with built-in short circuit current reduction," in *2011 20th European Conference on Circuit Theory and Design (ECCTD)*, 2011, pp. 142–145. DOI: 10.1109/ECCTD.2011.6043302
- [19] S.-M. Yoo, J. S. Walling, and et al., "A switched-capacitor RF power amplifier," *IEEE Journal of Solid-State Circuits*, vol. 46, no. 12, pp. 2977–2987, 2011.
- [20] K. Kim, J. Y. Kim, B. M. Moon, and S.-O. Jung, "A 6.9– μ m² 3.26-ns 31.25-fJ robust level shifter with wide voltage and frequency ranges," *IEEE Transactions on Circuits and Systems II: Express Briefs*, vol. 68, no. 4, pp. 1433–1437, 2021. DOI: 10.1109/TCSI.2020.3035188
- [21] R. Lotfi, M. Saberi, S. R. Hosseini, A. R. Ahmadi-Mehr, and R. B. Staszewski, "Energy-efficient wide-range voltage level shifters reaching 4.2 fJ/transition," *IEEE Solid-State Circuits Letters*, vol. 1, no. 2, pp. 34–37, 2018. DOI: 10.1109/LSSC.2018.2810606
- [22] J. Park and H. Jeong, "Energy-efficient wide-range level shifter with a logic error detection circuit," *IEEE Transactions on Very Large Scale Integration (VLSI) Systems*, vol. 31, no. 5, pp. 701–705, 2023.
- [23] A. A. Vatanjou and et al., "An ultra-low voltage and low-energy level shifter in 28-nm UTBB-FDSOI," *IEEE T. Circuits Syst. II*, vol. 66, no. 6, pp. 899–903, 2019.
- [24] S. Han and Y. Lee, "A complementary positive feedback-assisted current mirror-based level shifter for efficient wide voltage range operation," in *2024 IEEE European Solid-State Electronics Research Conference (ESSERC)*, 2024, pp. 613–616.